Processing and Application of Ceramics 19 [2] (2025) 139–149
https://doi.org/10.2298/

Effect of Sm^{3+} doping on the structural and electrical conduction in $PbTiO_3$ ceramics

Shyamanand Pandey[1,*], Sumit Kumar Roy[2], Swarat Chaudhuri[2]

[1]*University Department of Physics, Ranchi University, Ranchi-834001, Jharkhand, India*
[2]*Department of Physics, St. Xavier's College, Ranchi University, Ranchi-834001 Jharkhand, India*

Received 15 January 2025; Received in revised form 6 May 2025; Accepted 31 May 2025

Abstract

In the present study, lead titanate doped with 1 mol% Sm ($Pb_{0.985}Sm_{0.01}TiO_3$ - PST) was synthesized by using planetary ball mill and solid-state reaction method. The PST ceramics were obtained by sintering at 800, 900, 1000 and 1100 °C and their structure and electrical conductivity were investigated. The structural studies confirmed the presence of tetragonal phase and uniform fine grain structure of the prepared ceramics. It is observed that DC conductivity is directly proportional to temperature and follows the Arrhenius law. AC conductivity also increases with the increase in temperature for all sintered samples, but the σ_{AC} vs. frequency curves tend to become flat, which shows the dominance of DC conductivity at higher temperatures in the low frequency region. The variation of density of states (DOS) at the Fermi level with temperature at different frequencies was investigated for the PST ceramics. The experimental investigation of DOS was compared with computational studies using material simulation software Quantum Espresso for optimized geometry. The studies of DC and AC conductivity confirmed migration between long range potential wells of the charge carriers and polaron induced charge-hopping mechanism in these ferroelectric ceramics.

Keywords: *Sm-doped $PbTiO_3$, mechanochemical synthesis, conductivity, polaron hopping, density of states*

I. Introduction

One of the most important types of advanced materials for the research is the group of ferroelectric ceramics [1–3]. Perovskite oxide materials have chemical structure (ABO_3). The A-cation occupies the corner sites, the B-cation is located at the body centre site and oxygen anion is at the face centre sites of the unit cell [4]. These perovskite materials can be doped at the A-site and/or B-site with cations having different ionic radii depending on charge balance and tolerance factor [5–7]. Perovskite based ferroelectric materials have numerous applications viz. high capacity memory devices, catalyst, high temperature superconductors, optical waveguides, frequency based piezoelectric and pyroelectric devices, solid oxide fuel cells (SOFCs), sensors, solar cells, thermistors, etc. [8–12]. Studies on the partial substitution of cations at the A- and/or B-site in the perovskite structure indicate structural modifications, lattice distortions, cationic or anionic vacancies, change in oxidation state and may improve catalytic activity [13–16].

Rare earth doping at the A-site of the perovskite structure is widely investigated for their multifunctional applications [17–22]. Deren *et al.* [17] investigated cross relaxations of Ho^{3+} doped $CaTiO_3$ and $LaAlO_3$ perovskites for improvement of emission efficiency. Application in light emitting diodes (LEDs) is reported in the investigation of synthesis and photoluminescence of Eu^{3+}, Sm^{3+} and Pr^{3+} co-doped Ca_2ZnWO_6 double perovskite by Dabre *et al.* [18]. It was observed in the studies by Liang *et al.* [19] that La^{3+} doped $BaMnO_3$ has high stability and catalytic activity for CO and CH_4 oxidation. In another study by Li *et al.* [20], the partial substitution of Ce^{2+} by La^{3+} in the base compound $CeMnO_3$ acted as a catalyst and reduced NO to NH_3 at low temperatures. Sm^{3+} doped Srr_2NiMoO_6 double perovskite with the resultant structure $Sr_{2-x}Ni_xMoO_{6-\delta}$ can act as an anode material in SOFCs [21]. Singh *et al.* [22] have investigated the suitability of Sm^{3+} doped $SrTiO_3$ as an anode material in SOFCs. The conduction studies on the resultant perovskite structure $Sm_xSr_{1-x}TiO_{3-\delta}$ revealed polaron hopping with the formation of electrons.

There are various methods to synthesize rare earth

*Corresponding author: +91 9471506701
e-mail: *imshyam31@gmail.com*

doped perovskites, viz. wet chemical methods [23], solid state reaction method [24], spin-coating technique [25], pulsed laser deposition [26], electro-spinning technique [27], chemical vapour decomposition [28], etc. Wet chemical methods can be broadly classified into thermal decomposition [29], co-precipitation [30], sol-gel [31] and solvothermal methods [32]. Planetary ball mill (PBM) is an energy-intensive mechanochemical process used for synthesis of different compounds at nano-level [33,34].

The structure of lead titanate ($PbTiO_3$) is simple and easy to synthesize [35,36]. It is a promising material to investigate these days, used as ferroelectric and non-volatile information storage [37]. The properties of a large electro-optic coefficient and high photorefractive sensitivity make lead titanate (PT) an efficient optical sensor [38]. PT is enormously used in electronic industry for high temperature and frequency applications [39]. Though lead is graded as a toxic hazard, several researches indicate lead based oxides as an anticancer and antimicrobial drugs material [40,41]. PT ceramics are also used for the detection of cancerous hepatic tissues [42].

To the best of our knowledge, synthesis of Sm^{3+} doped PT by PBM and solid-state reaction method is reported for the first time. Previously Parashar *et al.* [43] have reported structural and electrical studies of Gd3+ doped PT synthesized by PBM. The authors have studied application of Nd^{3+} doped PT ferroelectrics in microelectronic memory devices. The phenomenon of the correlated barrier hopping (CBH) model was successful to explain experimental observations around morphotropic phase boundary (MPB) [44]. Chakraborty *et al.* [45] also investigated preparation of nano zinc titanate ceramics in spinel and perovskite form sintered at 800 °C using PBM. The electrical behaviour of the prepared ceramics was analysed through impedance spectroscopy [45].

The structural analyses through X-ray diffraction and scanning electron microscopy of Sm^{3+} doped PT were reported in the present investigation. The DC and AC components of electrical conductivity were evaluated as a function of temperature using complex impedance analysis [46]. The Jonscher's exponential constant S was calculated from the slope of $\log\sigma(\omega)$ vs. $\log\omega$ to explore the effect of polaron-induced temperature-dependent conduction phenomena in the prepared ceramics [47]. The conductivity data were further used to evaluate density of states (DOS) [43,44]. The optimized geometry, self-consistent-field (SCF) and DOS were calculated within the graphical user interface (GUI) of BURAI-1.3.1 of Quantum-Espresso (QE) software package [48,49].

II. Experimental

Lead titanate doped with 1 mol% Sm^{3+} ($Pb_{0.985}Sm_{0.01}TiO_3$ - PST) was synthesized by using planetary ball mill (PBM) and the solid state reaction method. The raw materials, PbO (99% from Merck), TiO_2 (99% from Merck) and Sm_2O_3 (99.9% from Sigma Aldrich) were mixed in stoichiometric ratio for 15 min. The stoichiometric chemical reaction for the desired compound is presented as follows:

$$0.985\,PbO + TiO_2 + 0.005\,Sm_2O_3 \longrightarrow \longrightarrow Pb_{0.985}Sm_{0.01}TiO_{3-\delta} + \frac{\delta}{2}O_2 \qquad (1)$$

The top-down synthesis approach was carried out in PBM using the high energy ball milling (HEBM) technique. The milling was performed in PBM (Retsch PM 200, Retsch, Germany) at room temperature for 0, 5, 10, 15 and 20 h. The milling process was conducted in a tungsten carbide (WC) vial and with WC balls with 10 mm diameter at a speed of 300 rpm and the ball-to-powder weight ratio of 20:1. The prepared ceramic powders were mixed with 3% of polyvinyl alcohol and then put in a hydraulic press with 20 bar applied pressure to obtain pellets of 12 mm diameter. For sintering, the samples were inserted in an electric furnace at 800, 900, 1000 and 1100 °C for 8 h.

The X-ray diffraction (XRD) patterns of the synthesized ceramics were recorded by using Rigaku D/Max 2200 with Cu Kα radiation (λ = 1.5406 Å) in the 20° to 80° 2θ range at a scanning rate of 0.020° min^{-1} for confirmation of phase composition. The crystallite size (D) of the prepared PST ceramics was calculated using the Scherrer's equation [50]:

$$D = \frac{0.89 \cdot \lambda}{\beta \cdot \cos\theta} \qquad (2)$$

where, λ = 0.154 nm is the wavelength of Cu Kα radiation, θ represents the Bragg's diffraction angle corresponding to the diffraction arising from a crystal plane and β is the full width at half maxima for a specific diffraction peak. The surface morphology of the Sm^{3+} doped $PbTiO_3$ ceramics has been analyzed using Scanning Electron Microscopy (SEM) HITACHI S-3400N with an air lock chamber.

In order to perform electrical characterization the flat polished surfaces of the sintered pellets were coated with silver paste (Alpha Aesar) and then dried at 600 °C for 30 min. The electrical parameters were measured using a HIOKI-3532 LCR Hitester under an electric field of about ~1 V in the temperature range of 100–525 °C at different frequencies varying from 10^2–10^6 Hz at a heating rate of 40 °C/min.

III. Results and discussion

3.1. Structural analysis

Figure 1a shows the XRD patterns (recorded at room temperature) of the prepared PST powders subjected to 5, 10, 15 and 20 h ball milling. It is evident that no sharp

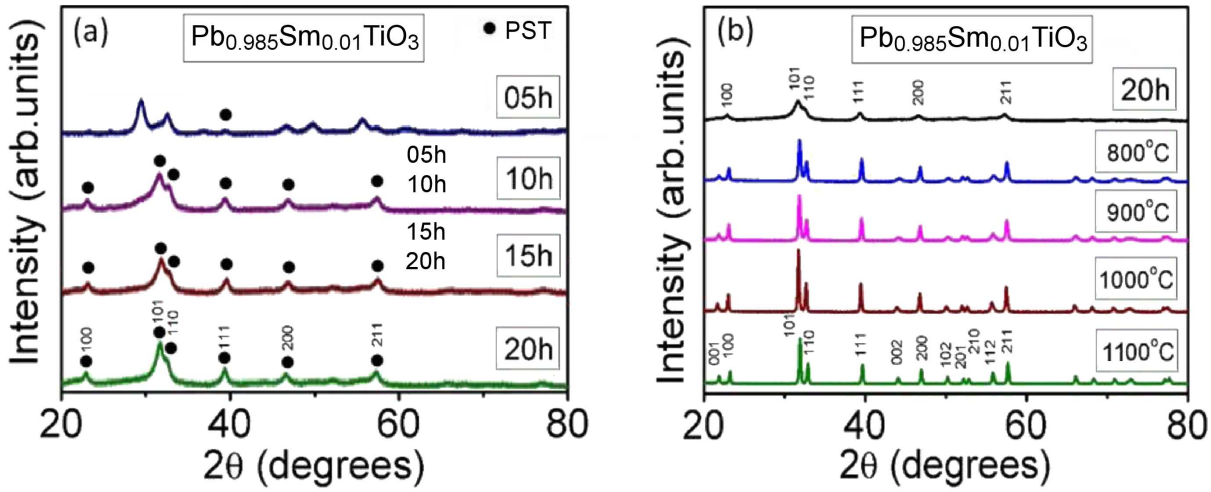

Figure 1. XRD patterns of: a) PST ceramics after 5, 10, 15 and 20 h of ball milling and b) PST ceramics subjected to 20 h of ball milling sintered at 800, 900, 1000 and 1100 °C for 8 h

peaks were present for the samples ball milled for 5 h. The definite pattern of XRD peaks gradually improves after 10 h of ball milling and prominent single phase peaks were observed after 20 h of ball milling.

The XRD patterns (Fig. 1b) of Sm^{3+} doped $PbTiO_3$ ceramics sintered at 800, 900, 1000 and 1100 °C matched the diffraction peaks of tetragonal PT phase identified using X-pert High Score plus. It can be seen from Fig. 1b that the prominent peaks are observed at ~31.9°, ~39.8° and ~58.7° which correspond to (101), (111) and (211) planes, respectively. The sharpness of the XRD peaks increases with the increase of sintering temperature. Thus, the large increase of the crystallite sizes of the Sm^{3+} doped $PbTiO_3$ samples (calculated using Eq. 2) was observed between the sample milled for 20 h (11.7 nm) and the sample heat treated at 800 °C (22.2 nm).

Grains, grain boundaries and pores are the parameters of ceramic microstructures [51], thus, microstructures of the prepared ceramics were analysed by SEM. It is evident from SEM micrographs shown in Fig. 2 that sintering improves the crystallinity of the prepared

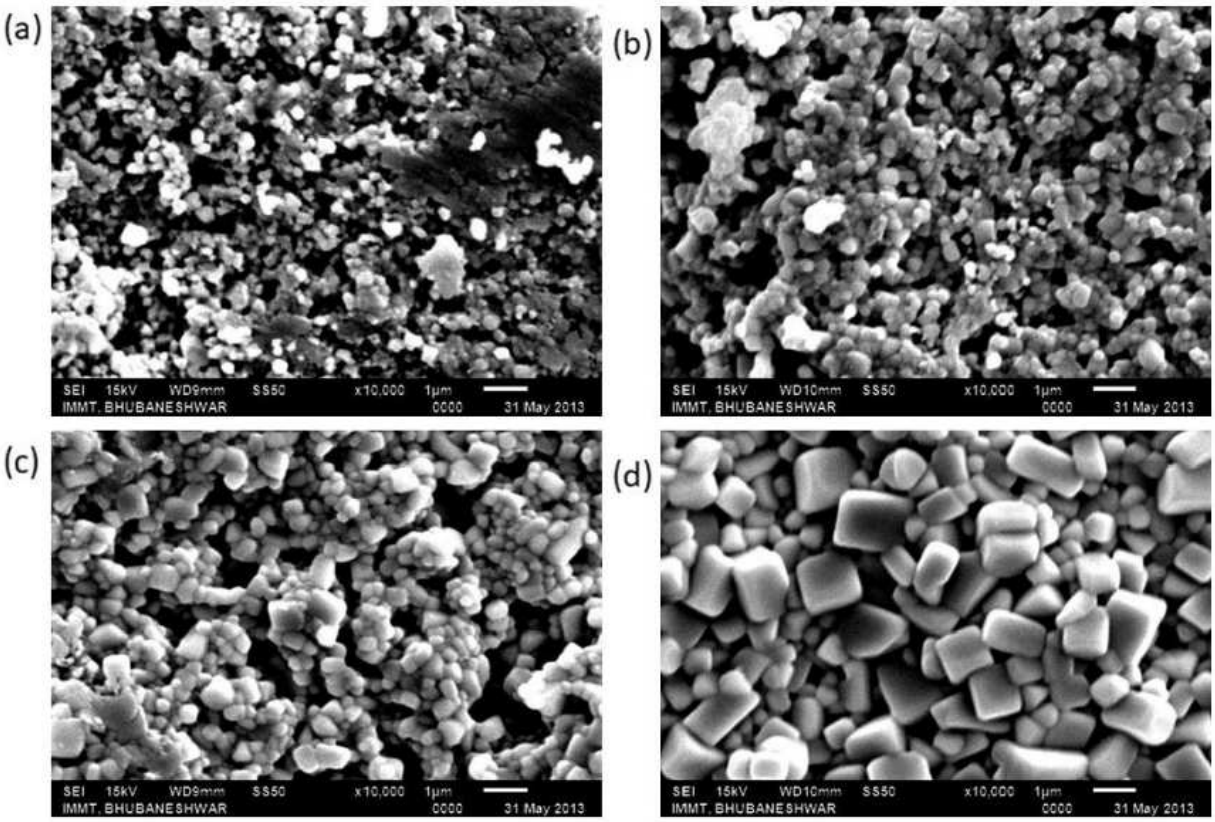

Figure 2. SEM micrographs of PST ceramics sintered at: a) 800 °C, b) 900 °C, c) 1000 °C and d) 1100 °C

ceramics. The grains are aggregated and deformed for the samples sintered at 800, 900 and 1000 °C, but the coarsening of the structure can be clearly seen. Uniformly distributed and relatively fine grains (the average grain size of ~1 μm) were observed for the PST sample sintered at 1100 °C. This may be due to the anisotropic growth rate along different crystal axes [52]. The lattice strains, calculated using POWD software [53] for the samples at RT, 800, 900, 1000 and 1100 °C, were 0.0183, 0.0107, 0.0101, 0.0047 and 0.0036, respectively. The porosity among the grains also decreases with the increase in sintering temperature. The degree of disorder for coarse grains is higher as compared to the fine-grained microstructures [54]. The increase in sintering temperature decreases entropy and porosity of the system, hence the transformation to the uniform fine grains structure was observed (Fig. 2d).

3.2. Conduction mechanism

DC electrical conductivity

The DC electrical conductivities of the PST ceramics sintered at 800, 900, 1000 and 1100 °C as a function of temperature are shown in Fig. 3. It is observed that DC conductivity (σ_{DC}) is directly proportional to the temperature and follows the Arrhenius law [55]:

$$\sigma = \sigma_0 \exp -\frac{E_a}{kBT} \tag{3}$$

where, σ_0 is the pre-exponential factor that depends on composition, E_a is the activation energy and T represent the absolute temperature. The activation energies of the PST samples sintered at 800, 900, 1000 and 1100 °C were obtained by linear fitting the measured conductivities presented in logarithmic plots (Fig. 3). The strong coupling of the dipoles in the ferroelectric region assists in thermally activated charge transport process [56]. It is clear from a literature survey that activation energies for singly and doubly ionized oxygen vacancies lie in the region of 0.3–0.6 eV and 0.7–0.12 eV respectively [57,58]. In the present investigation, the samples sintered at 800, 900, 1000 and 1100 °C have activation energies of 0.47, 0.48, 0.63 and 0.71 eV, respectively. Hence, it can be said that the samples sintered at 800, 900 and 1000 °C may have singly ionized oxygen vacancy and the sample sintered at 1100 °C doubly ionized oxygen vacancy. This may be accounted for by more conduction electrons and oxygen vacancies at higher sintering temperatures.

It is evident from Fig. 3 that E_a increases with sintering temperature. In crystalline ceramics, electrical conductivity is affected by bulk resistance (R_b) and grain boundary resistance (R_{gb}). The grain boundaries act as obstruction to the flow of charge carriers. With the increase of sintering temperature, R_b increases and R_{gb} decreases while grain size increases and grain boundaries become more ordered. This diverts the transfer of electron momentum and energy to the source of obstruction, which causes localized heating. Hence, higher activation energy is required to overcome these ordered grain boundaries [54,59].

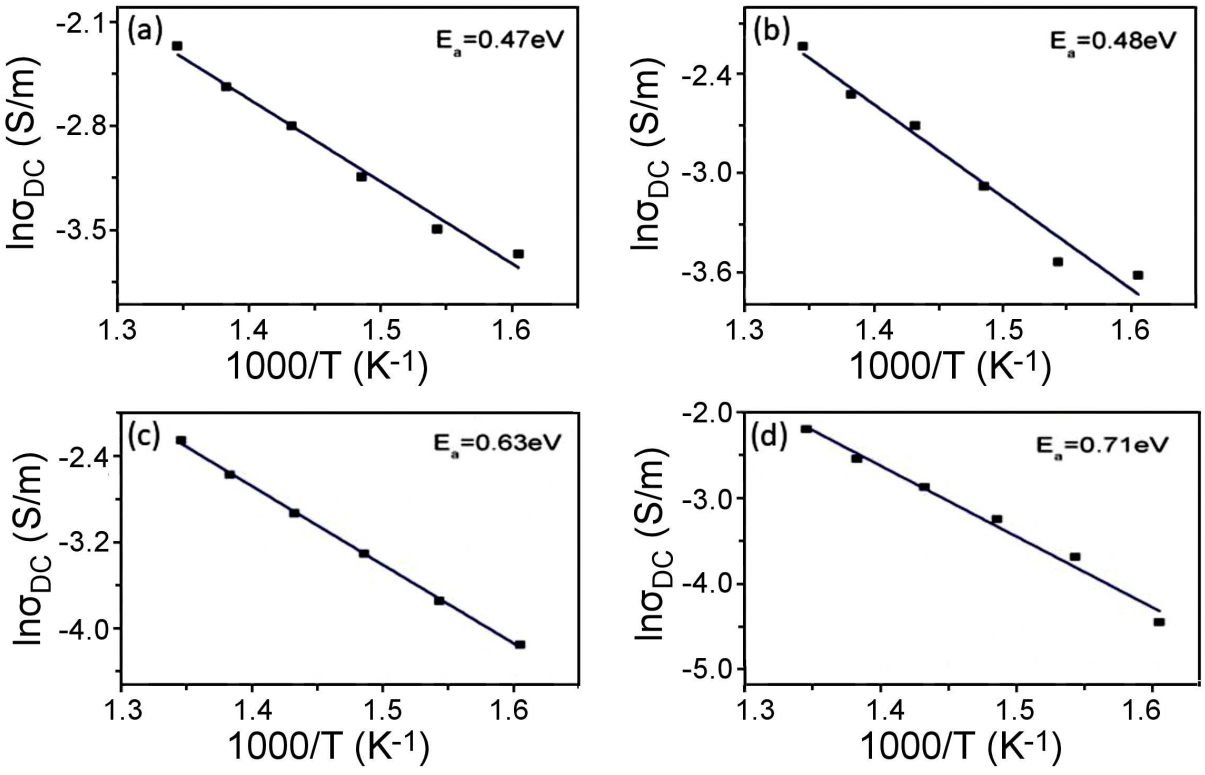

Figure 3. Variation of DC conductivity with inverse of temperature for PST ceramics sintered at: a) 800 °C, b) 900 °C, c) 1000 °C and d) 1100 °C

AC electrical conductivity

The frequency-dependent AC electrical conductivity in ceramics is often given by [60]:

$$\sigma_{AC} = \sigma_{DC} + A \cdot \omega^{S} \tag{4}$$

where σ_{DC} is DC part of conductivity, ω is the angular frequency of the applied field and S is the index of AC conductivity, which varies from $0 \leq S \leq 1$. The value of S is independent from ion-lattice and electron-lattice interactions. The constant factor A is given by the following equation:

$$A = \frac{\pi \cdot N^2 e^2}{6k_B \cdot T \cdot (2\alpha)} \tag{5}$$

where e is the electronic charge, T is the temperature, α is the polarizability of a pair of sites and N is the number of sites per unit volume among which hopping takes place. The factor A depends on the extent of polarization. The AC electrical conductivity in ceramics is often explained in terms of any of the following phenomena [61]: i) correlated barrier hopping (CBH), ii) quantum mechanical tunnelling (QMT), iii) non-overlapping small polaron tunnelling (NSPT) and iv) overlapping large polaron tunnelling (OLPT).

The AC electrical conductivities of the PST ceramics sintered at 800, 900, 1000 and 1100 °C are shown in Fig. 4. It is observed that σ_{AC} vs. frequency curves exhibit dispersion throughout the chosen frequency range, indicating relaxation behaviour in the prepared ceramics. With the increase of temperature for all the sintered samples, the curve tends to become flat, which shows the dominance of DC conductivity at higher temperatures in the low frequency region. It is evident from Fig. 4 that the magnitude of DC and AC conductivity increases with the increase in temperature, exhibiting the properties of negative temperature coefficient of resistance (NTCR) in the prepared ceramics [44,58]. The increase in AC conductivity is related to the hopping of bound carriers trapped in the crystalline samples. Such bound charge carriers at different lattice sites are often termed as polarons. There is a change in the slope of AC conductivity with frequency and it is related to the temperature at which the grain resistance dominates over grain boundary resistance [45,61].

The factor S was calculated using Jonscher's law from Eq. 4 and the obtained data are given in Fig. 5. It is found that S decreases with the increase of temperature for all the prepared ceramics. It is noticeable from Fig. 5 that the value of S tends toward zero at high temperatures in all the sintered samples which again indi-

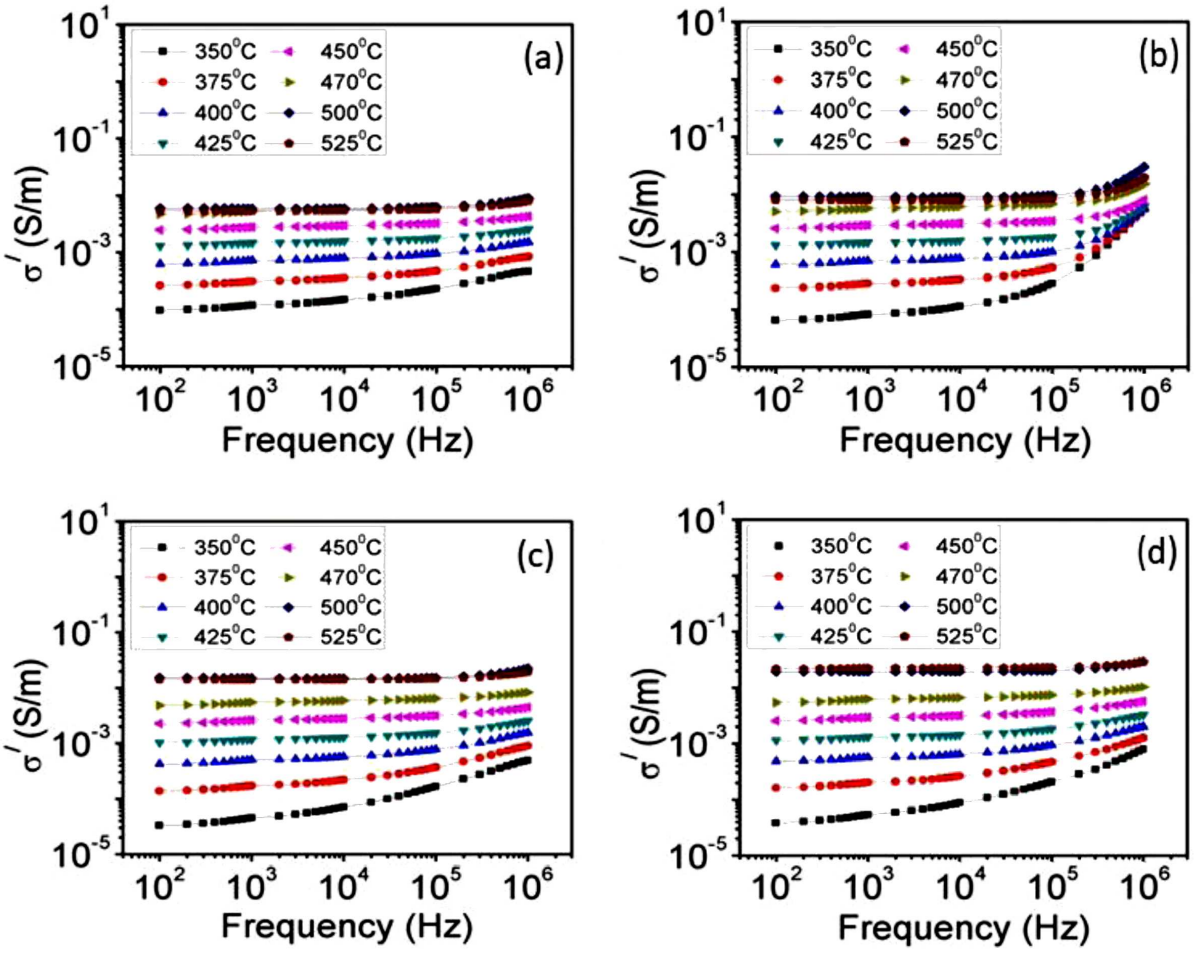

Figure 4. Variation of AC conductivity of PST with frequency at: a) 800 °C, b) 900 °C, c) 1000 °C and d) 1100 °C

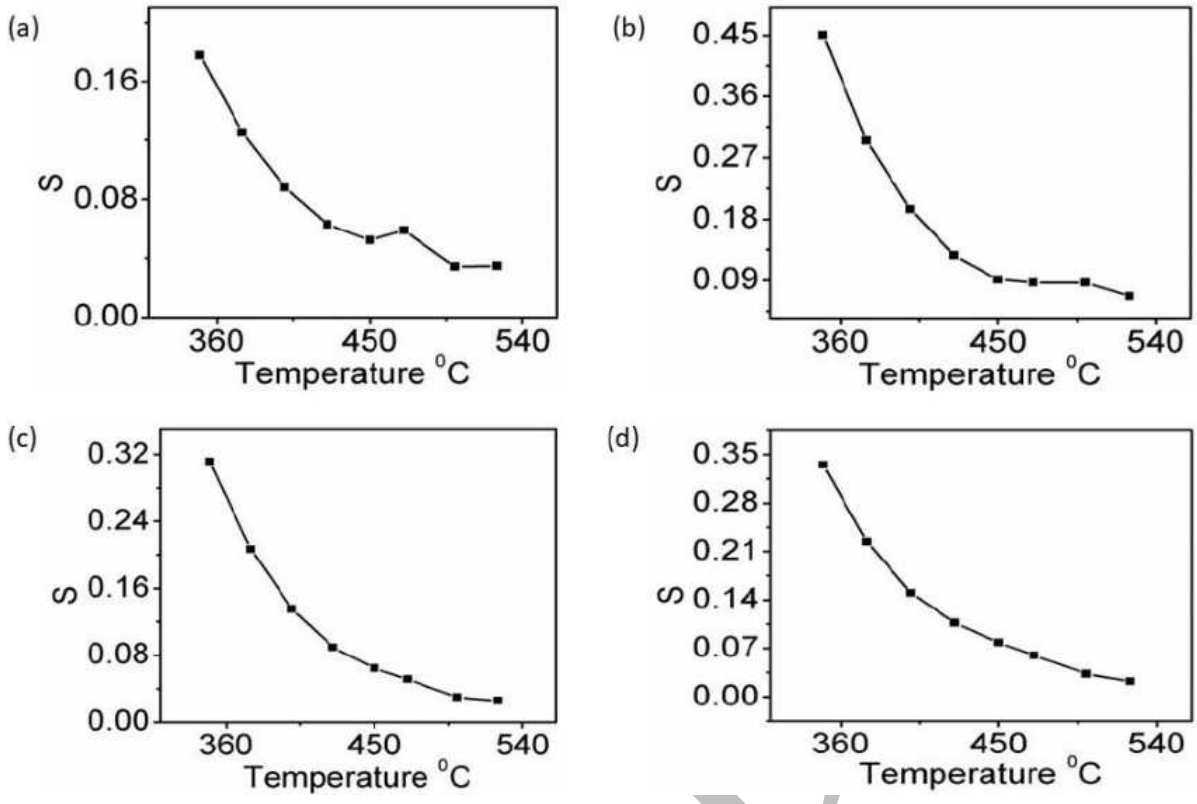

Figure 5. Variation of exponent *S* with temperature for PST ceramics sintered at: a) 800 °C, b) 900 °C, c) 1000 °C and d) 1100 °C

cates the dominance of DC conductivity at high temperatures [62]. The decrease in the value of *S* with temperature corresponds to the CBH model. Hence, the conduction process in the system is thermally activated. In Figs. 5a.b there is an abrupt change in the slope near MPB. This may be due to tunnelling of polarons with distortional overlap in the electron cloud of polarons. Hence, near MPB for the samples sintered at 800 and 900 °C, the OLPT mechanism is dominant although the CBH phenomenon exists in the entire temperature range. The slope of the curve gradually becomes horizontal with the increase of sintering temperature as observed in Figs. 5c,d. The temperature at which the slope change is observed corresponds to the polaron hopping of charged species. From SEM study it is clear that with the increase in sintering temperature of the prepared ceramics porosity decreases and grain size increases. Thus the grain boundary resistance and scattering of charged species decreases, hence motion of the charge carriers becomes much ordered which improves conductivity process in the system [63].

3.3. Density of states

The variation of density of states (DOS) at the Fermi level with temperature at four different frequencies (1, 10, 100 and 1000 kHz) for all the sintered samples is reported in Fig. 6. It is observed from literature survey that hopping conduction mechanism is usually consistent with the existence of high DOS in semiconductor ceramic materials [64]. This may be due to the localization of charge carriers and formation of polarons. It is clear from Fig. 6 that DOS increases with temperature for all frequencies and decreases after the phase transition temperature. This is ascribed to the transition from ferroelectric to paraelectric state [44]. With the increase in temperature dispersion behaviour is observed in all the prepared ceramics. This suggests variation in relaxation time between ionic and electronic polarizability. At low frequencies the electrical conduction in the system may be affected by both frequency as well as temperature, whereas at higher frequencies the charge carriers are localized and implicated by thermal excitations [45]. This experimental phenomena suggests CBH mechanism in the prepared samples. It is clear from SEM study (Fig. 2) that the higher sintering temperature increases grain size henceforth increasing the magnitude of DOS.

3.4. Computational studies

The Density Functional Theory (DFT) computations were performed using Quantum-Espresso [48,49] and the GUI module BURAI-1.3.1 was used to plot DOS. The vc-relax calculations for optimizations were done using Generalized Gradient Approximations-Perdew-Burke-Ernzerhof (GGA-PBE) exchange correlation functional [65]. The projector augmented wave method and Vanderbilt ultra-soft pseudopotentials were used to explain electron core interactions. The wave vectors (k) in the first Brillouin zone (4×4×4) were constructed using Monkhorst pack mesh scheme for self-

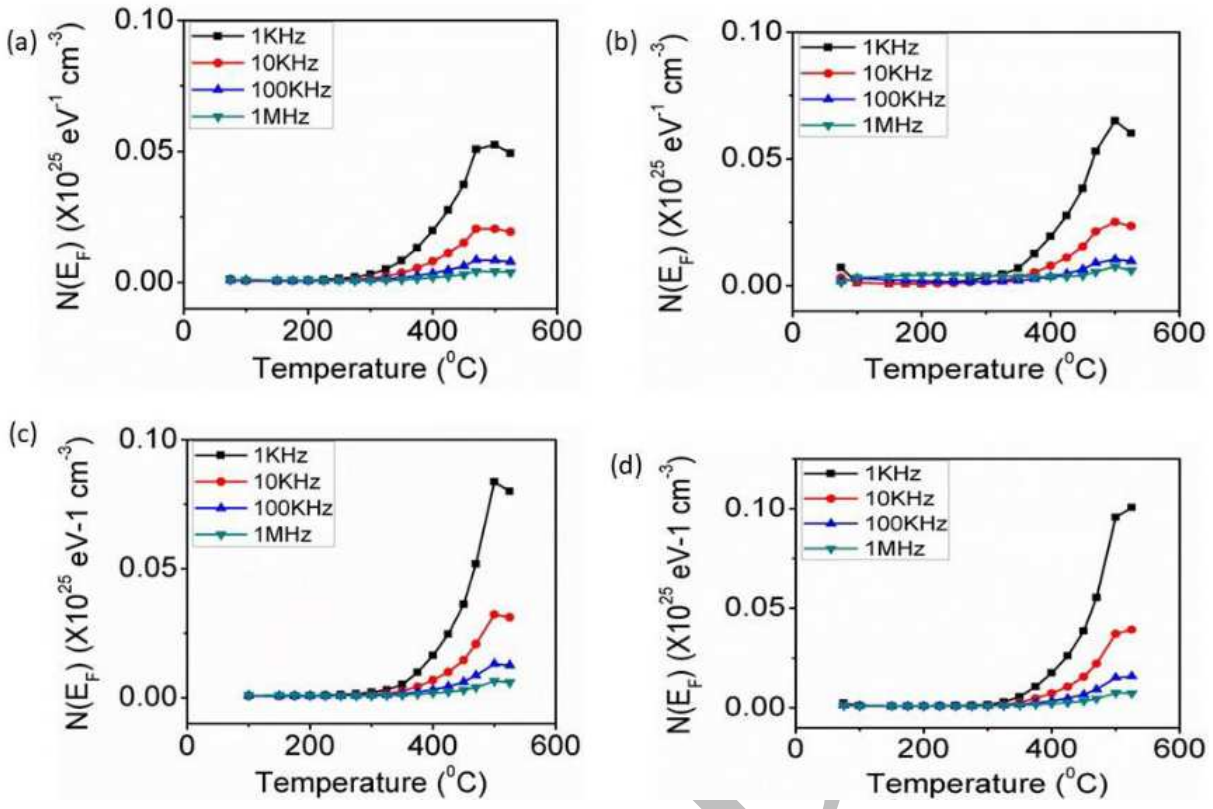

Figure 6. Experimental DOS at Fermi level with temperature at different frequencies for PST samples sintered at: a) 800 °C, b) 900 °C, c) 1000 °C and d) 1100 °C

consistent (SC) cycles [66]. The crystallographic XRD data of the prepared ceramic sintered at 1100 °C were used as initial lattice parameters for SC cycles as the crystal grains are prominent at 1100 °C. In our computation we have used kinetic energy cut-off at 46.69 Ry and charge cut-off at 323.02 Ry. The SC cycles converged after 24 iterations. The computed minimum ground state energy was found to be −380.19 Ry.

The DOS of the optimized PT and effect of dopant Sm^{3+} on the host PT in the form of DOS is elucidated in Fig. 7. The computation of DOS with respect to the energy is presented in the inset of Fig. 7b. The projected curves of up and down spins of the dopant Sm^{3+} nearly correspond to the total up and down spins of the total atoms in the optimized sample. The Fermi energy (E_F) is 0 eV in Fig. 7a and after doping with Sm^{3+} ion in the host material, E_F shifts towards the conduction band at 1.35 eV, as shown in Fig. 7b. When Sm^{3+} ion is doped at the A-site of the perovskite host $PbTiO_3$, the dopant Sm^{3+} acts as a donor impurity introducing excess electrons into the system. Also, the substitution of Pb^{2+} by Sm^{3+} ion creates a net positive charge. In order to maintain charge neutrality, electrons are introduced into the system. The host matrix is synthesized at a very high temperatures in the interval 800 to 1100 °C which can also lead to oxygen vacancies, acting as electron donors. This further increases the electron concentration, causing the Fermi energy to shift towards the conduction band. Due to this development, Sm^{3+} ion can modify the band structure of the base compound $PbTiO_3$, thereby

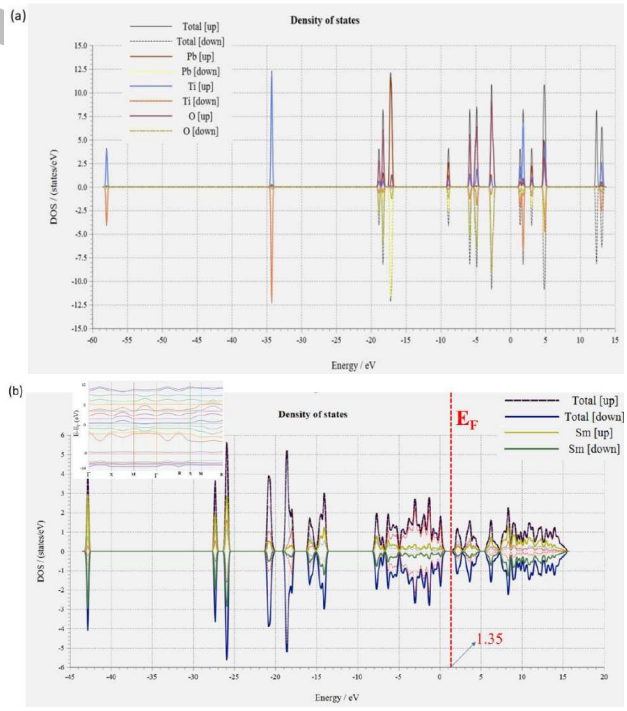

Figure 7. (a) DOS of the optimized PT; (b) Effect of Sm^{3+} doping of PT ceramics with respect to the total spin on DOS is elucidated using BURAI-1.3.1of QE. The inset shows the computed band structure of (E-E_F) in terms of eV represented by the high symmetry paths Γ-X-M-Γ-R-X-M-R in the first Brillouin zone

introducing new/altered energy levels of the existing ones. This can lead to the shift in the Fermi energy towards the conduction band and indicates that Sm^{3+} doping on the A-site of the perovskite structure has effective contribution on the electronic conductivity of the sample. There is overlap of DOS between −8 eV and 0 eV. This may be due to the strong hybridization of the *f*-orbitals of Sm with *d*-orbitals of Pb and/or oxygen atoms. The red curve in Fig. 7b corresponding to up-spin of oxygen atoms has high DOS below 0 eV and decreases after 2 eV whereas the DOS of Sm^{3+} increases manifold after 2 eV. The up and down spin of oxygen atoms becomes localized between ~5.1 eV and ~15.1 eV near ~0.2 DOS (states/eV). This may be due to shift in chemical bonding from Pb–O to Sm–O and Sm–Pb in the system. This is consistent with the studies reported by researchers about the change in Pb–O bonding about the phase transition of the prepared ceramic [67,68]. The valence band may be constructed due to the chemical interaction of the inner orbitals of Pb–O and Ti–O whereas in the conduction band the fermi orbitals of Sm–O, Pb–O and Sm–Pb are dominant [69].

Considering the ionic nature and separation by oxygen anions, direct chemical bonding between Sm^{3+} and Pb^{2+} ions is unlikely. However, Sm^{3+} and Pb^{2+} ions may interact through Coulomb's electrostatic forces, influencing the material's lattice parameters and stability. Sm^{3+} and Pb^{2+} ions may also be chemically bonded through shared anions affecting the material's electronic structure and properties. The effect of Ti–O bonding is portrayed in the inset of Fig. 7b. There is a sharp decrement in the value of DOS after the Fermi level (E_F) in the inset which corresponds to experimental DOS, reported in Fig. 6. In general Pb, Ti and oxygen must have +2e, +4e and −6e overall electronic charges in $PbTiO_3$ structure. The equilibrium of the electronic charges is maintained by delocalization of electrons and shift in chemical bonding from ionic to covalent bond between Pb–O and Sm–O atoms. The doping of Sm^{3+} in the Pb sites of the unit cell localize the electrons and leads to the formation of polarons. In order to compensate for the charge imbalance, oxygen vacancies are created in the perovskite structure [70,71]. It is the hopping of polarons in the vacant sites of oxygen at high temperature which drives to CBH mechanism in the prepared ceramics [72].

IV. Conclusions

$PbTiO_3$:Sm^{3+} (1 mol%) powder was synthesized by using high energy ball milling in the planetary ball mill and the PST ceramics were obtained by sintering at 800, 900, 1000 and 1100 °C. Single phase tetragonal structure was observed for the samples ball milled for 20 h. The increase in sintering temperature decreases entropy and porosity of the system, hence, transformation to the uniform fine grains structure was observed. Both DC and AC conductivities also increase with the increase in temperature for all sintered samples, but the σ_{AC} vs. frequency curves tend to become horizontal, which shows the dominance of the DC conductivity at higher temperatures in the low frequency region. The computation of DOS is in agreement with the experimental observations. The analysis of activation energies signifies oxygen vacancies in the prepared ceramics. The present study suggests conductivity of thermally activated polarons hopping over the Coulombic barrier separating defect centres in the prepared ceramics. As the prepared materials show NTCR behaviour, these samples can also be used to manufacture thermistors in electronic industry.

Acknowledgement: The authors express sincere thanks to the University Grants Commission (UGC), New Delhi, India for providing financial assistance in the form of Colleges with Potential for Excellence (CPE) status to St. Xavier's College, Ranchi, India (DO/21-49/2014/PE). One of the author Swarat Chaudhuri is also grateful to IMMT Bhubaneswar, Odisha, India for providing instrumentation facilities.

References

1. T. Parida, A. Kumar, B.S. Murty, G. Markandeyulu, "Magnetic and magnetoelectric response of Gd doped nickel ferrite and barium titanate nanocomposites", *J. Appl. Phys.*, **127** (2020) 114104.
2. K.H. Omran, M. Mostafa, M.S. Abd El-sadek, O.M. Hemeda, R. Ubic, "Effects of Ca doping on structural and optical properties of PZT nanopowders", *Results Phys.*, **19** (2020) 103580.
3. S. Zhou, D. Lin, Y. Su, L. Zhang, W. Liu, "Enhanced dielectric, ferroelectric, and optical properties in rare earth elements doped PMN-PT thin films", *J. Adv. Ceram.*, **10** (2021) 98–107.
4. M. Mostafa, Z.A. Alrowaili, G.M. Rashwan, M.K. Gerges, "Ferroelectric behavior and spectroscopic properties of La-Modified lead titanate nanoparticles prepared by a sol-gel method", *Heliyon*, **6** (2020) 03389.
5. D. Burnat, G. Nurk, L. Holzer, M. Kopecki, A. Heel, "Lanthanum doped strontium titanate - ceria anodes: deconvolution of impedance spectra and relationship with composition and microstructure", *J. Power Sources*, **385** (2018) 62–75.
6. J.P. Jwala, O. Subohi, M.M. Malik, "Influence of B-site modification by hetrovalent (Nb^{5+}) and isovalent (Zr^{4+}) dopants in $BaTiO_3$ on its dielectric and electrical properties synthesized by novel sol gel route", *Mater. Res. Express*, **6** (2019) 096308.
7. L.M. Daniels, S. Ling, S.N. Savvin, M.J. Pitcher, M.S. Dyer, J.B. Claridge, B. Slater, F. Corà, J. Alaria, M.J. Rosseinsky, "A and B site doping of a phonon-glass perovskite oxide thermoelectric", *J. Mater. Chem. A Mater.*, **6** (2018) 15640–15652.
8. E.A.R. Assirey, "Perovskite synthesis, properties and their related biochemical and industrial application", *Saudi. Pharm.*, **27** (2019) 817–829.
9. T. Wu, W. Pisula, M.Y.A. Rashid, P. Gao, "Application of perovskite-structured materials in field-effect transistors", *Adv. Electron, Mater.*, **5 [12]** (2019) 1900444.

10. Y. Tu, J. Wu, G. Xu, X. Yang, R. Cai, Q. Gong, R. Zhu, W. Huang, "Perovskite solar cells for space applications: Progress and challenges", *Adv. Mater.*, **33** [21] (2021) 2006545.
11. M. Chakraborty, V.K. Rai, V. Mishra, "Theoretical study on the zero field splitting and dopant position of Mn^{2+} in $KH_3(SeO_3)_2$ single crystal", *Optik*, **127** (2016) 4333–4338.
12. J. Yao, Q. Pan, Z.-J. Feng, Y.-A. Xiong, T.-T. Sha, H.-R. Ji, Z.-X. Gu, "Hybrid organic-inorganic perovskite ferroelectrics bring light to semiconducting applications: Bandgap engineering as a starting point", *APL Mater.*, **9** (2021) 040901.
13. W. Xia, Z. Pei, K. Leng, X. Zhu, "Research progress in rare earth-doped perovskite manganite oxide nanostructures", *Nanoscale Res. Lett.*, **15** (2020) 9.
14. Z. Chen, J. Hu, Z. Lu, X. He, "Low-temperature preparation of lanthanum-doped $BiFeO_3$ crystallites by a sol–gel-hydrothermal method", *Ceram. Int.*, **37** (2011) 2359–2364.
15. Y. Wen, C. Zhang, H. He, Y. Yu, Y. Teraoka, "Catalytic oxidation of nitrogen monoxide over $La_{(1-x)}Ce_xCoO_3$ perovskites", *Catal. Today*, **126** (2007) 400–405.
16. H. Taguchi, S. Yamasaki, A. Itadani, M. Yosinaga, K. Hirota, "CO oxidation on perovskite-type $LaCoO_3$ synthesized using ethylene glycol and citric acid", *Catal. Commun.*, **9** (2008) 1913–1915.
17. P. J. Dereń, K. Lemański, "Cross relaxation in $CaTiO_3$ and $LaAlO_3$ perovskite nanocrystals doped with Ho^{3+} ions", *J. Lumin.*, **154** (2014) 62–67.
18. K.V. Dabre, S.J. Dhoble, "Synthesis and photoluminescence properties of Eu^{3+}, Sm^{3+} and Pr^{3+} doped Ca_2ZnWO_6 phosphors for phosphor converted LED", *J. Lumin.*, **150** (2014) 55–58.
19. S. Liang, T. Xu, F. Teng, R. Zong, Y. Zhu, "The high activity and stability of $La_{0.5}Ba_{0.5}MnO_3$ nanocubes in the oxidation of CO and CH_4", *Appl. Catal. B*, **96** (2010) 267–275.
20. X. Li, Y. Yin, C. Yao, S. Zuo, X. Lu, S. Luo, C. Ni, "$La_{1-x}Ce_xMnO_3$/attapulgite nanocomposites as catalysts for NO reduction with NH_3 at low temperature", *Particuology*, **26** (2016) 66–72.
21. P. Kumar, S. Presto, A.S.K. Sinha, S. Varma, M. Viviani, P. Singh, "Effect of samarium (Sm^{3+}) doping on structure and electrical conductivity of double perovskite Sr_2NiMoO_6 as anode material for SOFC", *J. Alloys Compd.*, **725** (2017) 1123–1129.
22. S. Singh, R. Pandey, S. Presto, M.P. Carpanese, A. Barbucci, M. Viviani, P. Singh, "Suitability of Sm^{3+}-substituted $SrTiO_3$ as anode materials for solid oxide fuel cells: A correlation between structural and electrical properties", *Energies (Basel)*, **12** (2019) 4042.
23. Y. Zhou, J. Chen, O.M. Bakr, H.-T. Sun, "Metal-doped lead halide perovskites: Synthesis, properties, and optoelectronic applications", *Chem. Mater.*, **30**, (2018) 6589–6613.
24. O.B. Pavlovska, L.O. Vasylechko, I.V. Lutsyuk, N.M. Koval, Y.A. Zhydachevskii, A. Pieniążek, "Structure peculiarities of micro- and nanocrystalline perovskite ferrites $La_{(1-x)}Sm_xFeO_3$", *Nanoscale Res. Lett.*, **12** (2017) 153.
25. L. Wang, H. Zhou, J. Hu, B. Huang, M. Sun, B. Dong, G. Zheng, Y. Huang, Y. Chen, C.-H. Yan, "A Eu^{3+}- Eu^{2+} ion redox shuttle imparts operational durability to Pb-I perovskite solar cells", *Science*, **363** (2019) 265–270.
26. D. Preziosi, L. Lopez-Mir, X. Li, T. Cornelissen, J.H. Lee, F. Trier, K. Bouzehouane, S. Valencia, A. Gloter, A. Barthélémy, M. Bibes, M. Bib, "Direct mapping of phase separation across the metal-insulator transition of $NdNiO_3$", *Nano Lett.*, **18** [4] (2018) 2226–2232.
27. W. Zhang, H. Wang, Kai Guan, Z. Wei, X. Zhang, J. Meng, X. Liu, J. Meng, "$La_{0.6}Sr_{0.4}Co_{0.2}Fe_{0.8}O_{3-\delta}/CeO_2$ heterostructured composite nanofibers as a highly active and robust cathode catalyst for solid oxide fuel cells", *ACS Appl. Mater. Interfaces*, **11** [30] (2019) 26830–26841.
28. J. Schwarzkopf, D. Braun, M. Hanke, R. Uecker, M. Schmidbauer, "Strain engineering of ferroelectric domains in $K_xNa_{(1-x)}NbO_3$ epitaxial layers", *Front. Mater.*, **4** (2017) 26.
29. G. Pan, X. Bai, D. Yang, X. Chen, P. Jing, S. Qu L. Zhang, D. Zhou, J. Zhu, W. Xu, B. Dong, H. Song, "Doping lanthanide into perovskite nanocrystals: Highly improved and expanded optical properties", *Nano Lett.*, **17** (2017) 8005–8011.
30. S. Shi, L.-D. Sun, Y.-X. Xue, H. Dong, K. Wu, S.-C. Guo, B.-T. Wu, C.-H. Yan, "Scalable direct writing of lanthanide-doped $KMnF_3$ perovskite nanowires into aligned arrays with polarized up-conversion emission", *Nano Lett.*, **18** (2018) 2964–2969.
31. E. Devi, B.J. Kalaiselvi, K. Madhan, D. Vanidha, S.S. Meena, R. Kannan, "Quantification of charge carriers participating antiferromagnetic to weak ferromagnetic phase transition in Na doped $LaFeO_3$ nano multiferroics", *J. Appl. Phys.*, **124** (2018) 084102.
32. F.A. Rabuffetti, R.L. Brutchey, "Complex perovskite oxide nanocrystals: low-temperature synthesis and crystal structure", *Dalton Trans.*, **43** (2014) 14499–14513.
33. L.B. Kong, J. Ma, F. Boey, "Nanosized hydroxyapatite powders derived from coprecipitation process", *J. Mater. Sci.*, **37** (2002) 1131–1134.
34. S.K.S. Parashar, R.N.P. Choudhary, B.S. Murty, "Ferroelectric phase transition in $Pb_{0.92}Gd_{0.08}(Zr_{0.53}Ti_{0.47})_{0.98}O_3$ nanoceramic synthesized by high-energy ball milling", *J. Appl. Phys.*, **94** (2003) 6091–6096.
35. S. Shabanalizadeh, A. Abedini, A. Alborzi, M. Bahmani, N. Shaghaghi, S. Hajebi, M. Yazdanmehr, "Green synthesis and characterization of lead titanate nanoparticles and its photocatalyst application", *J. Mater. Sci. Mater. Electron.*, **27** (2016) 2589–2593.
36. M.A.E.-F. Gabal, "Synthesis and characterization of nanocrystalline $PbTiO_3$", *Ind. Eng. Chem. Res.*, **50** (2011) 13771–13777.
37. L. Liu, T. Ning, Y. Ren, Z. Sun, F. Wang, W. Zhou, S. Xie, L. Song, S. Luo, D.Liu, J. Shen, W. Ma, Y. Zhou, "Synthesis, characterization, photoluminescence and ferroelectric properties of $PbTiO_3$ nanotube arrays", *Mater. Sci. Eng. B*, **149** (2008) 41–46.
38. J.-M. Zhang, Q. Pang, K.-W. Xu, aV. Ji, "First-principles study of the (110) polar surface of cubic $PbTiO_3$," *Comput. Mater. Sci.*, **44** (2009) 1360–1365.
39. T.-Y. Chen, S.-Y. Chu, R.-C. Chang, C.-K. Cheng, C.-S. Hong, H.-H. Nien, "The characteristics of low-temperature sintered $PbTiO_3$ based ceramics and its applications", *Sens. Actuators A Phys.*, **134** (2007) 452–456.
40. W. Muhammad, M.A. Khan, M. Nazir, A. Siddiquah, S. Mushtaq, S.S. Hashmi, B.H. Abbasi, "*Papaver somniferum* L. mediated novel bioinspired lead oxide (PbO) and iron oxide (Fe_2O_3) nanoparticles: In-vitro biological

applications, biocompatibility and their potential towards HepG2 cell line", *Mater. Sci. Eng. C*, **103** (2019) 109740.
41. A. Miri, M. Sarani, A. Hashemzadeh, Z. Mardani, M. Darroudi, "Biosynthesis and cytotoxic activity of lead oxide nanoparticles", *Green Chem. Lett. Rev.*, **11** (2018) 567–572.
42. S. Laufer, A. Ivorra, V.E. Reuter, B. Rubinsky, S.B. Solomon, "Electrical impedance characterization of normal and cancerous human hepatic tissue", *Physiol. Meas.*, **31** (2010) 995–1009.
43. S. Parashar, S. Chaudhuri, S. Singh, M. Ghoranneviss, "Electrical conduction in nanoceramic PGT synthesised by high energy ball milling", *J. Theoret. Appl. Phys.*, **7** (2013) 26.
44. M. Chakraborty, S. Chaudhuri, V.K. Rai, V. Mishra, "Nd doped lead titanate crystals for microelectronic memory device applications", *J. Mater. Sci. Mater. Electron.*, **27** (2016) 7478–7486.
45. M. Chakraborty, V.K. Rai, K. Mitra, "Investigation on the electrical and optical properties of some zinc titanate ceramics," *Pramana*, **92** (2019) 46.
46. L.H. Omari, R. Moubah, A. Boutahar, L. Hajji, R. El Ouatib, "Analysis of electrical properties using complex impedance spectroscopy in solid solutions $(PbTiO_3)_{0.97}$-$(LaFeO_3)_{0.03}$ prepared by sol-gel technique", *J. Electroceram.*, **44** (2020) 23–31.
47. T. Mondal, S. Das, T.P. Sinha, P.M. Sarun, "Dielectric relaxation and study of electrical conduction mechanism in $BaZr_{0.1}Ti_{0.9}O_3$ ceramics by correlated barrier hopping model", *Mater. Sci.-Poland*, **36** (2018) 112–122.
48. P. Giannozzi, O. Andreussi, T. Brumme, O. Bunau, M. Buongiorno Nardelli, M. Calandra, R. Car, C. Cavazzoni, D. Ceresoli, M. Cococcioni, N. Colonna, I. Carnimeo, A. Dal Corso, S. de Gironcoli, P. Delugas, R.A. DiStasio Jr, A. Ferretti, A. Floris, G. Fratesi, G. Fugallo, R. Gebauer, U. Gerstmann, F. Giustino, T. Gorni, J. Jia, M. Kawamura, H-Y. Ko, A. Kokalj, E. Küçükbenli, M. Lazzeri, M. Marsili, N. Marzari, F. Mauri, N.L. Nguyen, H-V. Nguyen, A. Otero-de-la-Roza, L. Paulatto, S. Poncé, D. Rocca, R. Sabatini, B. Santra, M. Schlipf, A.P. Seitsonen, A. Smogunov, I. Timrov, T. Thonhauser, P. Umari, N. Vast, X. Wu, S. Baroni, "Advanced capabilities for materials modelling with QUANTUM ESPRESSO", *J. Phys. Condens. Matter*, **29** (2017) 465901.
49. P. Giannozzi, S. Baroni, N. Bonini, M. Calandra, R. Car, C. Cavazzoni, D. Ceresoli, G.L Chiarotti, M. Cococcioni, I. Dabo, A. Dal Corso, S. de Gironcoli, S. Fabris, G. Fratesi, R. Gebauer, U. Gerstmann, C. Gougoussis, A. Kokalj, M. Lazzeri, L. Martin-Samos, N. Marzari, F. Mauri, R. Mazzarello, S. Paolini, A. Pasquarello, L. Paulatto, C. Sbraccia, S. Scandolo, G. Sclauzero, A.P. Seitsonen, A. Smogunov, P. Umari, R.M. Wentzcovitch, "QUANTUM ESPRESSO: A modular and open-source software project for quantum simulations of materials", *J. Phys. Condens. Matter*, **21** (2009) 395502.
50. P. Scherrer, "Nachrichten von der Gesellschaft der Wissenschaften zu Göttingen", *Mathematisch-Physikalische Klasse*, **2** [1] (1918) 98–100.
51. Y. Ikuhara, "Grain boundary and interface structures in ceramics", *J. Ceram. Soc. Jpn.*, **109** (2001) S110–S120.
52. J-W. Lee, S-H. Bae, N.D. Marco, Y-T. Hsieh, Z. Dai, Y. Yang, "A review of experimental and computational attempts to remedy stability issues of perovskite solar cells", *Mater. Today Energy*, **7** (2018) 149.
53. E. Wu, "POWD An interactive powder diffraction data interpretation and indexing program", *School of Physical Science, Flinders, University of South Australia, Bedford Park, S.A., 5042, Australia*: 2.1.
54. M. Saber, C.C. Koch, R.O. Scattergood, "Thermodynamic grain size stabilization models: An overview", *Mater. Res. Lett.*, **3** (2015) 65–75.
55. K.J. Laidler, "The development of the Arrhenius equation", *J. Chem. Educ.*, **61** [6] (1984) 494.
56. E. Ricohermoso, F. Klug, H. Schlaak, R. Riedel, E. Ionescu, "Compressive thermal stress and microstructure-driven charge carrier transport in silicon oxycarbide thin films", *J. Eur. Ceram. Soc.*, **41** (2021) 6377–6384.
57. S. Sharma, V. Singh, O. Parkash, R.K. Dwivedi, "Effect of processing on dielectric properties of $(0.95)PbZr_{0.52}Ti_{0.48}O_3$–$(0.05)BiFeO_3$", *Appl. Phys. A*, **112** (2013) 975–984.
58. A. Chawla, A. Singh, M. Singh, P.S. Malhi, "Small polaron hopping-assisted electrical conduction and relaxation in BCT and Mn-doped BCT samples", *J. Asian Ceram. Soc.*, **7** (2019) 558–568.
59. D.K. Mahato, A. Dutta, T.P. Sinha, "Impedance spectroscopy analysis of double perovskite Ho_2NiTiO_6", *J. Mater. Sci.*, **45** (2010) 6757–6762.
60. A.K. Jonscher, "Dielectric relaxation in solids", *J. Phys. D Appl. Phys.*, **32** (1999) R57–R70.
61. S. Amhil, E. Choukri, S. Ben Moumen, A. Bourial, L. Essaleh, "Evidence of large hopping polaron conduction process in strontium doped calcium copper titanate ceramics", *Phys. B Condens. Matter*, **556** (2019) 36–41.
62. M.N.V. Ramesh, K.V. Ramesh, "Impedance spectroscopic studies of zirconium substituted $0.8BaTiO_3$ - $0.2Bi_{0.5}K_{0.5}TiO_3$ lead free ceramics", *Ferroelectrics*, **585** (2021) 178–186.
63. S. Behara, L. Ghatti, S. Kanthamani, M. Dumpala, T. Thomas, "Structural, optical, and Raman studies of Gd doped sodium bismuth titanate", *Ceram. Int.*, **44** (2018) 12118–12124.
64. A. Janotti, C. G. Van de Walle, "Fundamentals of zinc oxide as a semiconductor", *Reports Prog. Phys.,* **72** (2009) 126501.
65. J.P. Perdew, K. Burke, M. Ernzerhof, "Generalized gradient approximation made simple", *Phys. Rev. Lett.*, **77** (1996) 3865–3868.
66. L.Q. Chen, S.J. Xiao, L. Peng, T. Wu, J. Ling, Y.F. Li, C.Z. Huang, "Aptamer-based silver nanoparticles used for intracellular protein imaging and single nanoparticle spectral analysis", *J. Phys. Chem. B*, **114** (2010) 3655–3659.
67. S.R. de Lázaro, E. Longo, A. Beltran, J.R. Sambrano, "Propriedades eletrônicas e estruturais do $PbTiO_3$: teoria do funcional de densidade aplicada a modelos periódicos", *Quim. Nova*, **28** (2005) 10–18.
68. R. Salam, "Trapping parameters of electronic defectes states in indium tin oxide from AC conductivity", *Phys. Status Solidi A*, **1170** (1990) 535–540.
69. J. Dutta, M. Chakraborty, V.K. Rai, "Investigation on $ZnTiO_3$ codoped Er^{3+}/Yb^{3+} nanophosphors with enhanced upconversion emission and in temperature sensing application", *Optik*, **233** (2021) 166558.
70. A. Badreldin, A. E. Abusrafa, A. Abdel-Wahab, "Oxygen-deficient perovskites for oxygen evolution reaction in alkaline media: a review", *Emergent Mater.*, **3** (2020) 567–590.

71. H. Wang, B. Wang, Q. Li, Z. Zhu, R. Wang, C. H. Woo, "First-principles study of the cubic perovskites$BiMO_3$M Al , Ga, In, and Sc)", *Phys. Rev. B*, **75** (2007) 245209**.**
72. A. Alvermann, H. Fehske, S.A. Trugman, "Polarons and slow quantum phonons", *Phys. Rev. B*, **81** (2010) 165113.